Nano Energy 60 (2019) 743–751

ELSEVIER

Contents lists available at ScienceDirect

Nano Energy

journal homepage: www.elsevier.com/locate/nanoen

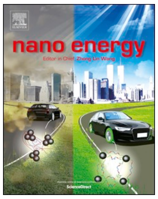

Full paper

Free-standing integrated cathode derived from 3D graphene/carbon nanotube aerogels serving as binder-free sulfur host and interlayer for ultrahigh volumetric-energy-density lithium−sulfur batteries

Haodong Shi[a,b,1], Xuejun Zhao[a,1], Zhong-Shuai Wu[a,*], Yanfeng Dong[a,c], Pengfei Lu[a], Jian Chen[a], Wencai Ren[d], Hui-Ming Cheng[d,e], Xinhe Bao[a,f]

[a] *Dalian National Laboratory for Clean Energy, Dalian Institute of Chemical Physics, Chinese Academy of Sciences, 457 Zhongshan Road, Dalian, 116023, China*
[b] *University of Chinese Academy of Sciences, 19 A Yuquan Road, Shijingshan District, Beijing, 100049, China*
[c] *Department of Chemistry, College of Sciences, Northeastern University, 3-11 Wenhua Road, Shenyang, 110819, China*
[d] *Shenyang National Laboratory for Materials Science, Institute of Metal Research, Chinese Academy of Sciences, 72 Wenhua Road, Shenyang, 110016, China*
[e] *Tsinghua-Berkeley Shenzhen Institute, 1001 Xueyuan Road, Shenzhen, 518055, China*
[f] *State Key Laboratory of Catalysis, Dalian Institute of Chemical Physics Chinese Academy of Sciences, 457 Zhongshan Road, Dalian, 116023, China*

ARTICLE INFO

Keywords:
Graphene
Compact film
Integrated cathode
Ultrahigh volumetric energy density
Lithium sulfur batteries

ABSTRACT

The actual applications of lithium sulfur (Li—S) batteries are significantly obstructed by limited cyclability and low volumetric-energy-density due to the shuttling effect of polysulfides and low mass density of sulfur cathode. Herein, we report a free-standing, compact, conductive and integrated cathode (G/CNT-S//G/CNT), constructed by compressing graphene/carbon nanotubes (G/CNT) aerogels, simultaneously serving as bi-functionalities of binder- and metal-current-collector-free sulfur host (G/CNT-S) and interlayer (G/CNT), for high volumetric-energy-density Li—S batteries. The G/CNT aerogels display three-dimensional interconnected porous network, large surface area (363 $m^2 g^{-1}$) and high electrical conductivity (67 $S m^{-1}$), which can endow the cathode with ultrahigh volumetric mass density (1.64 $g cm^{-3}$) and superior electron-ion transport network. Meanwhile, the compressed ultralight G/CNT film can act as flexible interlayer for synergistically suppressing the polysulfide shuttling via both chemical interaction and physical restriction. Consequently, the compact cathodes, achieve high capacity of 1286 mAh g^{-1} at 0.2 C and long-term cyclability with an extremely low decay rate of 0.06% over 500 cycles at 2 C. Most importantly, our compact cathodes represent unprecedented volumetric capacity of 1841 Ah L^{-1} and volumetric-energy-density of 2482 Wh L^{-1}, both of which are the highest values of Li—S batteries reported to date. Therefore, this proposed strategy will open a new avenue for developing high volumetric-energy-density Li—S batteries.

1. Introduction

The ever-increasing demand of electric vehicles, portable electronics, and grid applications has unprecedentedly promoted the continuous development of cost-efficient advanced batteries with high energy density and long-term cyclability. Lithium-sulfur (Li—S) batteries, as one highly competitive alternative for commercially available lithium ion batteries, have drawn considerable attentions on account of high theoretical capacity (1675 mAh g^{-1}), gravimetric (2600 Wh kg^{-1}) and volumetric (2800 Wh L^{-1}) energy density, and low-cost of naturally abundant and non-toxic elemental sulfur [1–6]. However, the practical applications of Li—S batteries have been significantly hampered by several issues, including intrinsically poor electrical conductivities of sulfur (5×10^{-30} $S cm^{-1}$) and discharge products Li_2S_2/Li_2S [7–9], large volume expansion (78.7%) of sulfur particle during cycling [10], and shuttling effect of lithium polysulfides (Li_2S_x, $4 \le x \le 8$) [5,11–13], all of which result in low capacity, rapid capacity degradation and limited cyclability of Li—S batteries [14].

To address these issues, various strategies have been proposed, such as elaborated design of high-sulfur loading hosts (e.g., porous carbon [15–17], hollow carbon spheres [18], carbon nanotube (CNT) [19–21], graphene [22–24], carbon hybrids [25,26], conducting polymers [27], metal oxides [28–30], and metal or covalent organic frameworks [31–33]), cathodic protective layers [34], interlayers positioned

---

[*] Corresponding author.
E-mail address: wuzs@dicp.ac.cn (Z.-S. Wu).
[1] H.D. Shi and X.J. Zhao contributed equally to this work.

https://doi.org/10.1016/j.nanoen.2019.04.006
Received 23 February 2019; Received in revised form 1 April 2019; Accepted 1 April 2019

between cathode and separator [35–37], organosulfides [38], and metal polysulfides (e.g., TiS_4 [39], MoS_3 [40], FeS_2 [41], VS_4 [42]). It is noted that, taking into account of actual applications, the integration of nano sulfur into nanocarbon hosts is more reliable and inexpensive, which can sufficiently endow sulfur with high electrical conductivity and provide enough space for sulfur loading and volume change. The introduction of effective interlayer between the cathode and separator can greatly suppress the diffusion of lithium polysulfides by chemical interaction and physical blocking, as well as catalytic oxidation of Li_2S, leading to enhanced capacity and cyclability [43].

Besides, one key issue lies in the low mass densities of both nano sulfur (2.07 g cm^{-3}) and porous carbon host, usually generating low volumetric capacity of cathode and limited volumetric-energy-density of the whole cell. Therefore, how to attain high volumetric density without sacrifice of high gravimetric energy density of Li—S batteries is becoming one of the biggest challenges we are facing [44]. In general, most porous carbon/sulfur cathodes were assembled by a traditional slurry-casting process, in which the use of metal current collector (e.g., Al foil), conductive agent and polymer binders inevitably decrease volumetric-energy-density of Li—S batteries. To this end, one reliable and efficient strategy is to construct the binder-free compact, conductive, free-standing and integrated cathode combining the sulfur host with interlayer together for Li—S batteries. As a typical example, Cheng's group fabricated an all-graphene integrated cathode, with porous graphene as high-loading sulfur host, highly conductive graphene as internal current collector, and partially oxygenated graphene as suppressing interlayer, for high-performance Li—S batteries [45]. Xiang et al. fabricated nitrogen-doped carbon foam/sulfur cathode decorated with reduced graphene oxide (rGO) interlayer, exhibiting enhanced capacity and rate capability [46]. Despite the great progress, the construction of mixed electron-ion conductive and integrated cathode with high volumetric performance and long-term cyclability for Li—S batteries still remains elusive.

Herein, we develop high volumetric-energy-density and long-life Li—S batteries based on the free-standing, densely compact, mixed electron-ion conductive, and integrated cathode (denoted as G/CNT-S//G/CNT), derived from three-dimensional (3D) interconnected porous graphene/CNT (G/CNT) aerogels, simultaneously serving as sulfur host (G/CNT-S) and interlayer (G/CNT). The 3D G/CNT aerogels are fabricated by self-propagating combustion rapid reduction of graphene oxide/CNT (GO/CNT) aerogels, and present 3D interconnected porous network, large surface area of 363 $m^2 g^{-1}$, and high electrical conductivity of 67 S m^{-1}, which can serve as a superior sulfur host. Meanwhile, the G/CNT aerogels based compact film can act as ultralight internal current-collector interlayer, which can hinder the shuttling effect of lithium polysulfides *via* synergistically both chemical interaction and physical restriction. What's more, the cross-link CNT endow ultrahigh volumetric sulfur loading cathode with superior ion and electron transport network. As a consequence, the as-assembled integrated cathode manifests high reversible capacity of 1286 mAh g^{-1} at 0.2 C, and exceptionally long-term cycling stability with an extremely low decay rate of 0.06% over 500 cycles at 2 C. Furthermore, our G/CNT-S//G/CNT cathode shows the highest volumetric capacity of 1841 Ah L^{-1}, volumetric-energy-density of 2482 Wh L^{-1} and power density of 496 W L^{-1} for Li—S batteries reported to date.

2. Experimental

2.1. Preparation of 3D G/CNT aerogels

GO was firstly synthesized by the modified Hummers' method [47]. After that, 20 mL GO suspension (10 mg mL^{-1}) and 2 mL multi-walled CNT (1 mg mL^{-1}) were mixed together, and sonicated for 2 h. Then, the resulting concentrated suspension was freeze-dried in polystyrene Petri dishes for 3 days to obtain 3D GO/CNT aerogels (diameter: 40 mm). Finally, the 3D GO/CNT aerogels were rapidly reduced by simply exposing it to the fire by a lighter at ambient condition, and the 3D GO/CNT aerogels rapidly self-propagated and spontaneously extended from the initial fire spot to the whole aerogel in seconds to form 3D G/CNT aerogels.

2.2. Fabrication of G/CNT-S//G/CNT cathode

The G/CNT-S aerogels were prepared by immersing G/CNT aerogels into sulfur-containing carbon disulfide solution (100 mg mL^{-1}), and thus heating at 155 °C for 12 h in Ar atmosphere. Then, the G/CNT-S aerogels were pressed at different pressures (10, 20, 30 MPa) to obtain the G/CNT-S compact film as sulfur-based cathodes. For the interlayer, the 3D G/CNT aerogels were directly pressed to form ultralight G/CNT compact film which is only 0.2 mg cm^{-2}. Finally, the above G/CNT-S and G/CNT films were assembled together to form the compact integrated G/CNT-S//G/CNT cathode.

2.3. Permeation measurements

The Li2S6 solution (0.1 M) was prepared by mixing sulfur and Li_2S with a molar ratio of 5:1 into appropriate amount of THF by vigorously stirring at 50 °C until the sulfur was fully dissolved. Afterwards, the Li_2S_6 solutions and pure THF solution were separated using the PP separator (Celgard 2400, pore diameter of 0.2 μm, and thickness of 25 μm) or G/CNT interlayer/PP separator (thickness of 15.2 μm). Meanwhile, the photographs were taken at 0, 3 and 12 h, respectively.

2.4. Material characterization

The morphology and structure of materials were characterized by SEM (JEOL JSM-7800F), TEM (JEM-2100), atomic force microscope (AFM, Veeco nanoscope multimode II-D), XPS (Thermo ESCALAB 250Xi equipped with monochromatic Al Kα source of 1486.5eV), FT-IR (Bruker, Hyperion 3000), XRD (Empyrean with Cu Kα radiation in the 2θ range from 5 to 90°), thermogravimetric analysis (TGA, SDT Q600 V20.9 Build 20), Raman spectroscopy (LabRAM HR 800 Raman spectrometer, 632 nm). Nitrogen adsorption and desorption isotherm was carried out to investigate the specific surface area, pore size distribution, and pore volume of the products. Electrical conductivity was measured by a standard four-point probe system (RTS-9).

2.5. Electrochemical measurement

The electrochemical performance of Li—S batteries was conducted using CR2016 coin cells with lithium foil as the counter and reference electrodes. CR2016 coin cells were assembled in argon-filled glove box with water and oxygen content below 0.5 ppm. The G/CNT-S//G/CNT electrode was cut into thin circular plates with diameter of 12 mm as working electrode. The electrolyte was 1.0 M lithium bis(trifluoromethanesulfonyl) imide (LiTFSI) in a mixture solution of 1,3-dioxolane (DOL) and 1,2-dimethoxyethane (DME) (1:1, vol. ratio) with 1 wt% $LiNO_3$ as additive, and the PP membrane (Celgard 2400) is used as the separator and the amount of electrolyte was controlled as around 40 μL for each cell. The cells were firstly discharged to 1.7 V, then cycled between 1.7 and 2.8 V at the different rates. The GCD profiles were performed using a LAND CT2001A battery system. CV curves were carried out on a CHI 760E electrochemical workstation at a scan rate of 0.1 mV/s. EIS were carried out using a CHI 760E workstation by applying an ac amplitude of 5 mV over the frequency range of 100 kHz to 0.01 Hz.

The electrode density is calculated from the mass and volume of the whole cathode, as shown in the following equation (1).

$$\rho = \frac{m_{\text{sulfur}} + m_{\text{carbon electrode}}}{V_{\text{cathode}}} \tag{1}$$

where ρ is the electrode density (g cm^{-3}), $m_{\text{carbon elctrode}}$ is the mass of the carbon host (g), m_{sulfur} is the mass of sulfur (g), V_{cathode} is the electrode volume (cm^3).

The volumetric energy ensity E_v and volumetric power density P_v are calculated according to the following equations (2) and (3).

$$E_v = \rho \cdot Q \cdot U \tag{2}$$

$$P_v = \frac{E_v}{\Delta t} \tag{3}$$

where Q is the discharge capacity (mAh g^{-1}), U is the average discharge plateau (V), Δt is discharged time (h) [48].

2.6. Computational simulation

All calculations were performed with $DMol^3$ module, which is integrated in Materials Studio 6.0 package [49,50]. The graphene sheets substituted by hG, eG, cG groups, respectively, were selected as the graphene surface models, and S-containing clusters (Li_2S_6) was considered as the adsorbate during the calculations. In the framework of density functional theory, the generalized gradient approximation combined with the Perdew-Burke-Enzerhof functional was employed to describe the exchange and correlation potential [51,52]. The structural relaxations of graphene and Li_2S_6 were carried out firstly, followed by the adsorption simulation step. All electrons were considered when tackling the electron-ion interactions for atoms in the whole system. The cutoff was set to 400 eV and k-points mesh in the Monkhorst Pack sampling scheme was set as $1 \times 1 \times 1$ [53]. For the convergence criteria, the self-consistent field tolerance used was 1.0×10^{-5} eV/atom, the maximum force and displacement were set as 5.0×10^{-2} eV/Å and 2.0×10^{-3} Å, respectively. The binding energy (E_{ads}) is defined as the energy difference between the surface model with Li_2S_6 molecule (E_{tot}) and the summation of Li_2S_6 molecule (E_1) and surface system (E_2): $E_{\text{ads}} = E_1 + E_2 - E_{tot}$.

3. Results and discussion

The fabrication of G/CNT-S//G/CNT integrated cathode is schematically illustrated in Fig. 1a. First, the uniform suspensions of GO (Fig. S1) and multi-walled CNT (Fig. S2) was obtained, and then freeze-dried to form 3D cross-linked GO/CNT aerogels, showing a golden yellow cylinder (Fig. 1b). After that, 3D GO/CNT aerogels were rapidly reduced to 3D G/CNT aerogels by self-propagating combustion (Fig. 1c). Notably, 3D interconnected porous networks were well kept after reduction (Fig. 1d, Fig. S3) due to the strongly cross linking of the wrinkled graphene and CNT (Fig. 1e). The colour change from golden yellow to dark indicated the efficient reduction (Fig. 1c). This was further confirmed by Fourier transform infrared spectroscopy (FT-IR, Fig. 1f), in which most oxygenated groups, e.g., at 3679–3000 cm^{-1} (OH), 2919 and 2848 cm^{-1} (C–H), 1727 cm^{-1} (C=O), 1627 cm^{-1} (COO^-), and 1039 cm^{-1} (C–O) were fully removed [54], as well as Raman spectra revealing the increased intensity ratio (I_D/I_G) of D band and G band from 0.92 for GO/CNT to 0.85 for G/CNT aerogels (Fig. 1g) [55]. Then, the G/CNT-S compact electrode was readily prepared by sufficient immersion of high-loading sulfur into large surface area and macroporous G/CNT aerogels (Fig. 1h), followed by low-temperature annealing and mechanical compression at 20 MPa. It is worth noting that this mechanical compression is of great importance to overcome the low mass density of G/CNT aerogels to form free-standing and compact films, and remarkably increase the total pore volume from 1.0 cm^3 g^{-1} for pristine G/CNT aerogels to 1.9 cm^3 g^{-1} for compact G/CNT film, and correspondingly achieve the porous structure transition from macropores to mesopores (25.6 nm, Fig. 1i). Importantly, such mesoporous feature in G/CNT film would greatly facilitate the ion diffusion, and offer enough space for volume change of nano sulfur and sufficient absorption of lithium polysulfides [56]. Meanwhile, 3D G/CNT aerogels were also pressed to form ultralight G/CNT compact film as the interlayer (0.2 mg cm^{-2}) which is negligible to the overall mass specific capacity for the cells. Finally, the resulting G/CNT-S host and G/CNT interlayer was assembled together to attain flexible, compact and integrated G/CNT-S//G/CNT cathode for Li–S batteries.

To highlight the importance of CNT and structure superiority of G/CNT aerogels over graphene aerogels serving as sulfur host and interlayer, we further applied the similar procedure to assemble S-containing graphene aerogels (denoted as G-S) derived film host without addition of CNT, and compared their mechanical flexibility and electrochemical performance. It is observed that the G/CNT-S film represented outstanding flexible properties without the appearance of structure cracks under different bending angles (Fig. 2a and b), however, the G-S film showed the obvious film fractures and limited flexibility (Fig. S4), demonstrative of the importance of cross-link CNT for enhancing structure stability (Fig. S5a). Cross-section scanning electron microscopy (SEM) image of G/CNT-S film displayed uniformly and densely compact structure, abundant of wrinkles, and a typical thickness of ~15.2 μm under 20 MPa (Fig. 2c). Notably, no bulk sulfur particles were found in the framework (Fig. S5b), allowing for uniform distribution and high loading up to 50 wt% of nano sulfur into the G/CNT aerogels (Fig. S6). This was further validated by energy dispersive X-ray (EDX) mapping, showing homogeneous element distribution of C, O, and S in the G/CNT-S film (Fig. 2d). Meanwhile, the G/CNT-S films represented impressively electrical conductivity of 67 S m^{-1}, superior to G-S film (25 S m^{-1}, Fig. 2e). Besides, X-ray diffraction (XRD) patterns further unveiled the shifting characteristic (002) peak from 11° to 23°, indicative of efficient reduction of GO (Fig. 2f, Fig. S7). Observably, the characteristic peaks of both G/CNT and S (JCPDS no. 42–1238) were appeared in G/CNT-S film without any impurities, indicative of the successful loading of nano sulfur into G/CNT framework (Fig. 2f). High resolution X-ray photoelectron spectroscopy (XPS) of C1s and S2p showed C–O/C–S bonds centered at 285.9 eV (Fig. 2g) [57], and S $2p_{3/2}$ peak (S–C) at 163.7 eV, and S $2p_{1/2}$ peak (S–O) at 168.5 eV (Fig. 2h) [58]. The existence of the C–O/C–S species verified the strong bonding of S with oxygen and carbon atoms in G/CNT-S film, indicative of strong anchoring of nano sulfur on carbon surface for enhancing the cyclability of Li–S batteries.

The electrochemical performances of the integrated cathodes of G/CNT-S//G/CNT and G-S//graphene aerogels interlayer (denoted G-S//G) for Li–S batteries were firstly compared. The initial four cyclic voltammetry (CV) curves of G/CNT-S//G/CNT electrode, tested in 1.7–2.8 V at 0.1 mV/s, showed negligible current changes and potential shifts in these CV peaks, and their shapes are almost overlapped (Fig. 3a), indicative of high electrochemical reversibility. In a sharp contrast, the G-S//G cathode represented obvious evolution of both current and potential (Fig. S8) with repeated cycles. Fig. 3b compared the CV curves of G/CNT-S//G/CNT and G-S//G cathodes. It can be observed that both of them presented two redox peaks, corresponding to the phase transitions from solid S_8 to liquid high-order Li_2S_x ($4 \le x \le 8$) at high potential, and from soluble Li_2S_x to solid Li_2S/Li_2S_2 at low potential [59]. Notably, the G/CNT-S//G/CNT cathode, in comparison with G-S//G, displayed well-defined redox peaks with higher peak currents, indicative of rapid conversion kinetics via the introduction of high conducting CNT. Furthermore, galvanostatic charge and discharge curves (GCD) profiles of G/CNT-S//G-CNT delivered higher capacity of 1234 mAh g^{-1} at 0.2 C, about four times higher than that of G-S//G electrode (310 mAh g^{-1} at 0.2 C, Fig. 3c), accompanied with remarkably enhanced rate capability (Fig. S9), further demonstrative of the structure superiority of G/CNT-S//G-CNT over G-S//G cathode. It can be well explained by electrochemical impedance spectroscopy (EIS, Fig. 3d), in which G/CNT-S//G-CNT displayed a smaller semicircle with charge-transfer resistance (R_{ct}) of 63.9 and 27.0 Ω before and after 10th cycle in the high-frequency region, much lower than those of G-S//G film (283.1 and 44.6 Ω before and after 10th cycle), suggesting enhanced mass-transfer process (Fig. 3d, and Fig. S10) [60]. Moreover, it is calculated that G/CNT-S//G/CNT

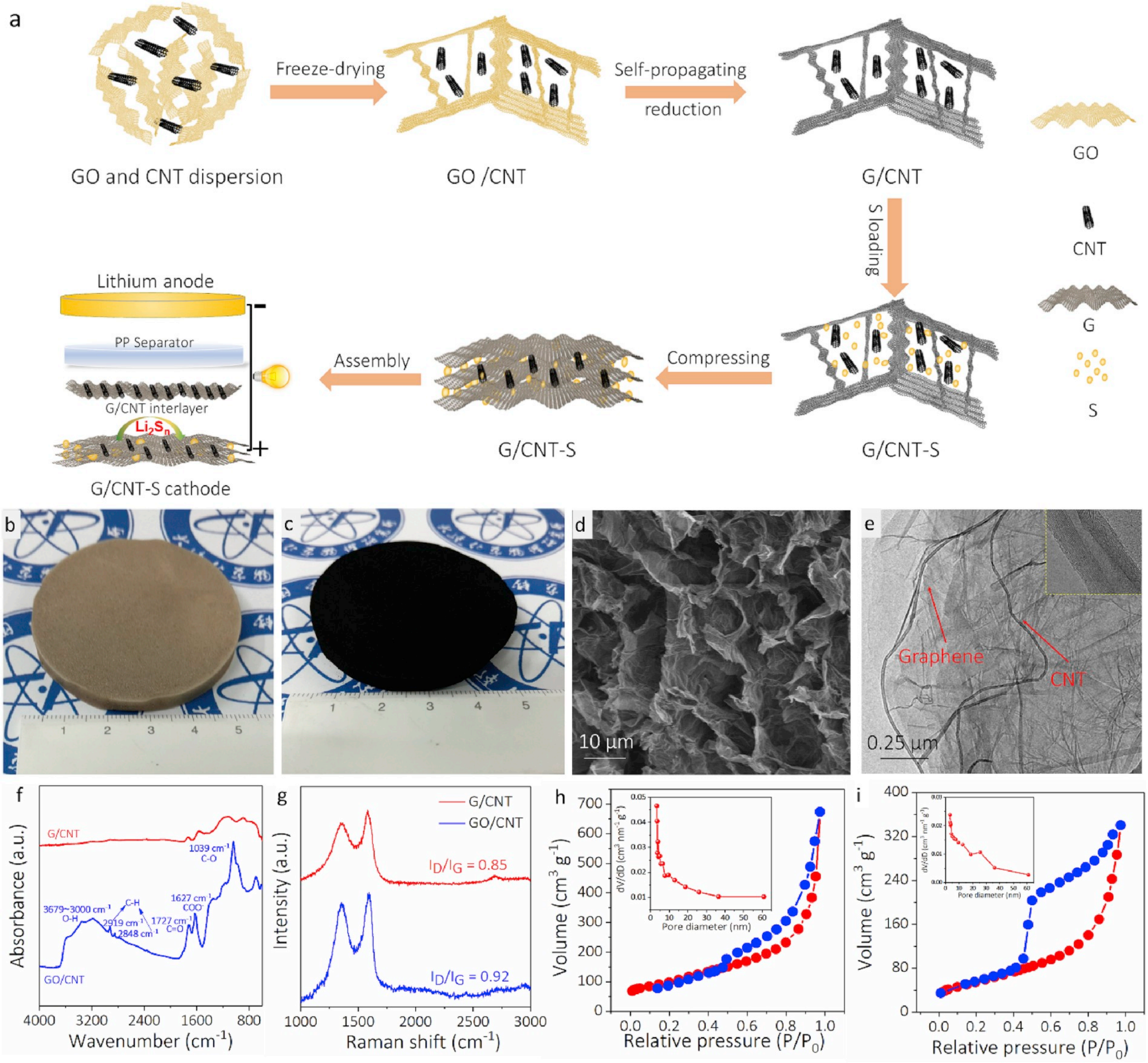

Fig. 1. (a) Schematic of the synthesis of G/CNT-S//G/CNT cathode integrated G/CNT-S host with G/CNT interlayer for Li—S batteries. (b, c) Photographs of (b) 3D GO/CNT aerogels and (c) G/CNT aerogels. (d) SEM image of G/CNT aerogels. (e) TEM image of G/CNT aerogels. Inset is HRTEM image of one multi-walled CNT on graphene. (f) FT-IR, and (g) Raman spectra of GO/CNT and G/CNT aerogels. (h, i) N_2 adsorption-desorption isotherms of (h) pristine and (i) pressed G/CNT aerogels. Insets are the plots of pore size distributions.

exhibited higher Li ion diffusion coefficient of $7.3 \times 10^{-10}\ cm^2\ s^{-1}$, nearly five times of G-S//G ($1.4 \times 10^{-10}\ cm^2\ s^{-1}$, Fig. 3e, Table S1) [61].

Furthermore, the pressure-dependent thickness of G/CNT-S//G/CNT cathode plays an important role in determining the performance of Li—S batteries (Fig. 3f and g). For instance, the thickness of G/CNT-S//G/CNT cathodes compressed at 10 MPa, 20 MPa and 30 MPa is 22.2, 15.2 and 14.5 μm, respectively (Fig. 2c, and Fig. S11). Notably, the cathode pressed at 20 MPa, tested at 0.5 C, exhibited higher reversible capacities of 1128 mAh g^{-1} and 1615 Ah L^{-1} than those obtained at 10 MPa (859 mAh g^{-1}, 842 Ah L^{-1}) and 30 MPa (918 mAh g^{-1}, 1378 Ah L^{-1}). After 40 cycles, the 20 MPa-pressed cathodes maintained larger capacity of 1070 mAh g^{-1} and 1531 Ah L^{-1} than the cathodes pressed at 10 MPa (725 mAh g^{-1}, 711 Ah L^{-1}) and 30 MPa (773 mAh g^{-1}, 1160 Ah L^{-1}) (Fig. 3h). In addition, the appropriate mass ratio (100:1) of graphene and CNT in integrated electrode is also of great importance to maximize the capacity and enhance cyclability of Li—S batteries (Fig. S12).

To demonstrate the importance of G/CNT interlayer in improving the Li—S performance, we further compared the electrochemical properties of G/CNT-S//G/CNT integrated cathode with G/CNT-S electrode without use of G/CNT interlayer, measured at varying current densities from 0.2 to 2 C. Remarkably, the G/CNT-S//G/CNT displayed higher initial capacity of 1286 mAh g^{-1} (1841 Ah L^{-1}) than that of G/CNT-S (1047 mAh g^{-1}) at 0.2 C. When increasing the current density, higher capacities of 990 mAh g^{-1} at 0.5 C (12th cycle), 732 mAh g^{-1} at 1 C (22nd cycle), and 493 mAh g^{-1} at 2 C (32nd cycle) were achieved, in comparison with G/CNT-S, e.g., 736 mAh g^{-1} at 0.5 C (12th cycle), 484 mAh g^{-1} at 1 C (22nd cycle), and 269 mAh g^{-1} at 2 C (32nd cycle) (Fig. 4a and b, Fig. S13). Importantly, after abruptly switching the current density back to 0.2 C, the integrated cathode still retained high capacity of 1027 mAh g^{-1} (52nd cycle), indicative of outstanding capacity retention (Fig. 4c). What's more, G/CNT-S//G/CNT showed impressively coulombic efficiency nearly 100% (Fig. S14), and importantly, the performance of G/CNT-S//G/CNT was also superior to most reported cathodes using carbon-based interlayers (Table S2).

In order to examine the main factor influencing rate capability of both G/CNT-S//G/CNT and G/CNT-S cathodes, two key parameters, the high and low-voltage plateau capacities are obtained from the discharge voltage profiles, denoted as Q_H and Q_L, were introduced to

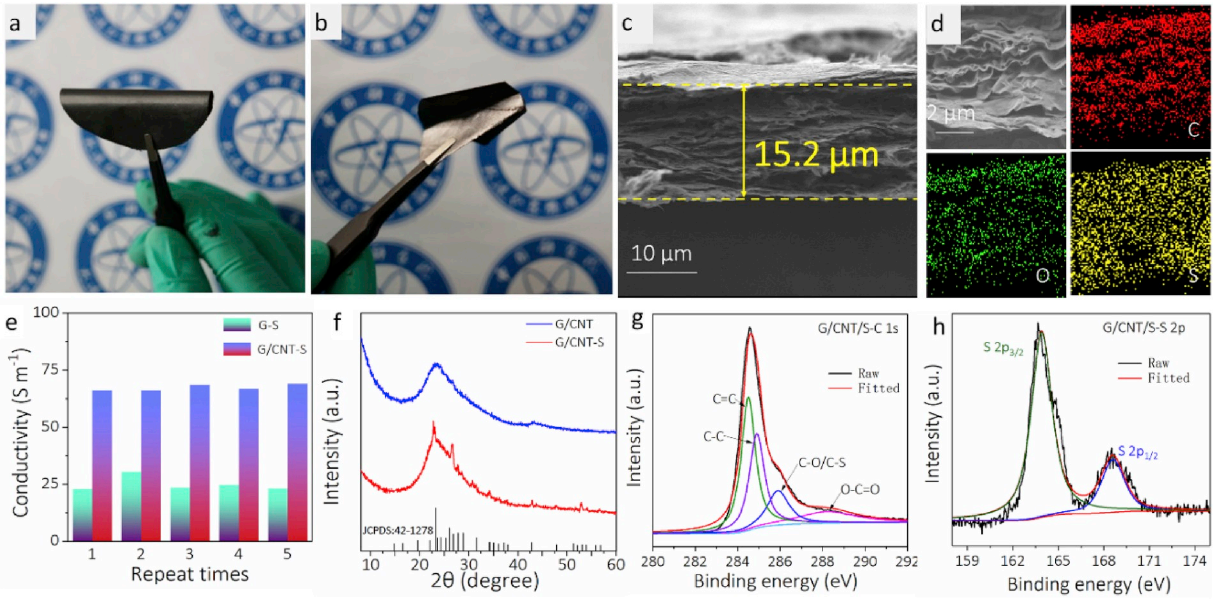

Fig. 2. (a, b) Photographs of G/CNT-S films taken under different bending angles. (c) Cross-section SEM image of G/CNT-S film compressed at 20 MPa. (d) EDX elemental mapping of carbon (red), oxygen (green) and sulfur (yellow). (e) Electrical conductivity of G/CNT-S and G-S films. (f) XRD patterns of G/CNT and G/CNT-S. (g) C1s and (h) S2p XPS spectra of G/CNTs-S films.

study the Li^+/e^- transport in the cathode (Fig. 4a and b). During low-voltage plateau, the insoluble Li_2S_2 and Li_2S species will generate and, thereby, apparently increase the resistance of Li^+/e^- transportation. Hence, the value of Q_L/Q_H can well reflect the ability of Li^+/e^- transport in the cathode [62]. It is revealed that the values (2.62–1.05) of Q_L/Q_H obtained from the cell assembled with G/CNT interlayer are higher than those without interlayer (2.17–1.01) at all rates (Fig. 4d). Moreover, the plateau of G/CNT-S//G/CNT was flatter and more stable with a low polarization of 223 mV at 0.2 C, while in the case of G/CNT-S cathode, a bigger voltage hysteresis of 407 mV was attained (Fig. 4e), suggestive of enhanced interfacial kinetics and Li^+/e^- transport due to the presence of interlayer. As a consequence, G/CNT-S//G/CNT, with high S loading of 2.46 mg cm^{-2}, still displayed high initial capacity of 1343 mAh g^{-1}, coulombic efficiency of almost 100%, and exceptionally enhanced cyclability (Fig. 4f and g) with capacity retention of 92% after 100 cycles at 0.5 C. In a sharp contrast, G/CNT-S electrode only showed an initial capacity of 425 mAh g^{-1} at 0.5 C and low coulombic efficiency of 95% (Fig. S15). It is deduced that the G/CNT interlayer could effectively restrict the shuttling effect of soluble lithium polysulfides, and then greatly boost the capacity and cyclability. To highlight the structure merit of flexible and compact cathode, we further compared the volumetric capacity vs volumetric sulfur loading of G/CNT-S//G/CNT film with the state-of-the-art cathodes for Li—S batteries (Fig. 4h and Table S3). Obviously, our G/CNT-S//G/CNT represented the highest volumetric capacity of 1615 Ah L^{-1} and volumetric sulfur loading of 1.64 g cm^{-3} for Li—S battery cathodes reported so far.

Furthermore, our G/CNT-S//G/CNT cathode exhibited excellent long-term cyclability upon 500 cycles at 2 C, delivering ~445 mAh g^{-1}

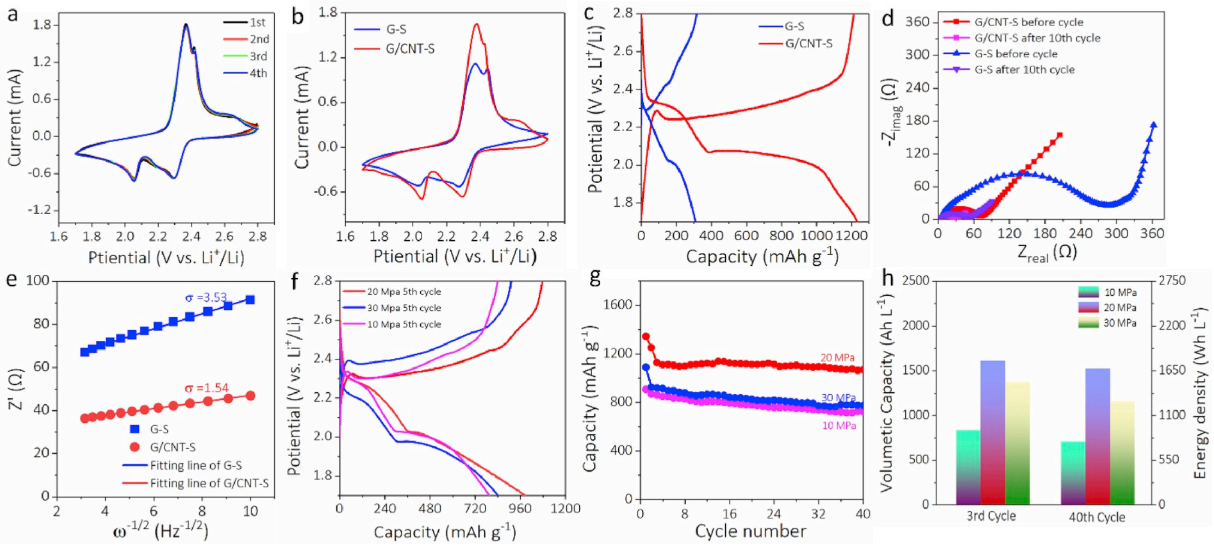

Fig. 3. (a) CV curves of G/CNT-S//G/CNT electrode measured at the initial four cycles, tested 0.1 mV/s (b) CV curves of G/CNT-S//G/CNT and G-S//G cathodes, measured at 0.1 mV/s (c) GCD profiles of G/CNT-S//G/CNT and G-S//G cathodes cycled at 0.2 C. (d) EIS of G/CNT-S//G/CNT and G-S//G cathodes. (e) Relationship of between *Z'* and the square root of the frequency ($\omega^{-1/2}$) in the low-frequency region. (f) GCD profiles and (g) cycling stability tested at 0.5 C of G/CNT-S//G/CNT cathodes, pressed at 10 MPa, 20 MPa and 30 MPa, respectively. (h) Comparison of volumetric capacity and volumetric energy density of G/CNT-S//G/CNT cathode, based on mass of the G/CNT-S electrode, obtained at 3rd and 40th cycles under different pressure.

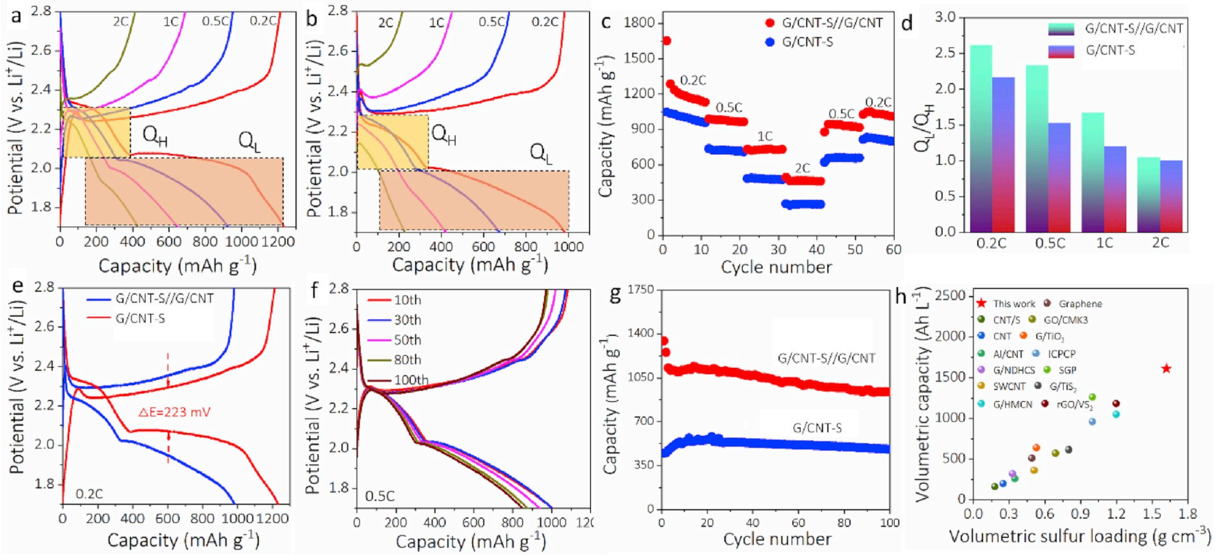

Fig. 4. (a, b) GCD profiles of (a) G/CNT-S//G/CNT and (b) G/CNT-S cathodes, measured from 0.2 to 2 C. (c) rate capability, (d) Q_L/Q_H values obtained at different rates, and (e) GCD profiles obtained at 0.2 C of G/CNT-S//G/CNT and G/CNT-S cathodes. (f) GCD profiles of G/CNT-S//G/CNT, tested at 0.5 C. (g) Cycling stability of G/CNT-S//G/CNT and G/CNT-S cathodes, obtained at 0.5 C. (h) Comparison of volumetric capacity vs volumetric sulfur loading of G/CNT-S//G/CNT cathodes with the currently reported cathodes.

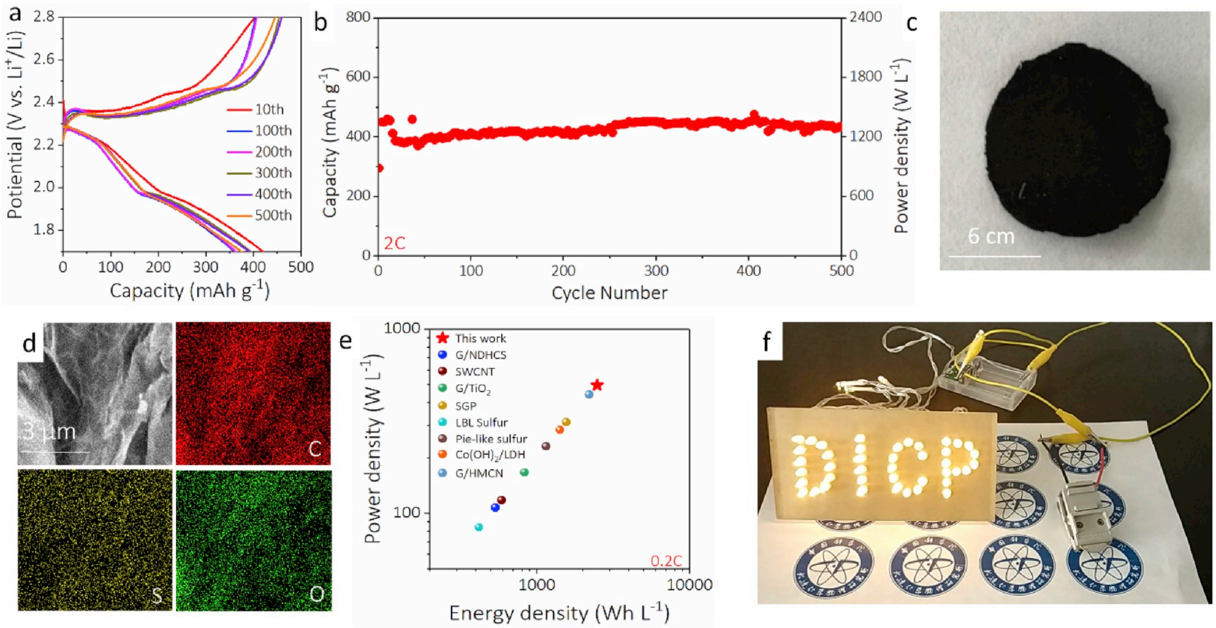

Fig. 5. (a) GCD profiles and (b) cycling stability of G/CNT-S//G-CNT cathode, measured at 2 C. (c) Photograph, and (d) SEM image and corresponding EDX elemental mapping of carbon (red), oxygen (green) and sulfur (yellow) of G/CNT interlayer after 500 cycles, tested at 2 C. (e) Ragone plot of G/CNT-S//G-CNT cathode in comparison with the state-of-the-art cathodes, obtained at 0.2 C. (f) Photograph of the "DICP" letters composed of 42 LED arrays, powered by two serially-connected Li—S batteries.

with an extremely low decay rate of 0.06% per cycle (Fig. 5a, b). Impressively, the G/CNT-S//G/CNT could still maintain the structure integrity well and display notable mechanical flexibility even at a bending state (Fig. 5c, Fig. S16). And the elemental mappings revealed homogeneous distribution of sulfur species in the G/CNT interlayer (Fig. 5d), which definitely trapped the migrating polysulfides between the host and interlayer, and then facilitated the efficient re-utilization of sulfur. A Ragone plot is shown in Fig. 5e to compare the G/CNT-S cathode with the recently reported cathodes, measured at 0.2 C. Remarkably, our G/CNT-S//G/CNT offered outstanding volumetric-energy-density of 2483 Wh L^{-1} and power density 497 W L^{-1}, both of which are much higher than those of the reported Li—S battery cathodes (Table S4), such as porous carbon nanofiber paper (420 Wh L^{-1}, 84 W L^{-1}) [63], graphene/TiO$_2$ (833 Wh L^{-1}, 167 W L^{-1}) [64], nano S graphene/PEDOT: PSS (1562 Wh L^{-1}, 313 W L^{-1}) [65], graphene/mesoporous carbon (2205 Wh L^{-1}, 441 W L^{-1}) [66]. Besides, two serially-connected Li—S coin-type cells with G/CNT-S//G/CNT cathodes can readily power the tandem 42 light-emitting diode (LED) array of "DICP" letters for more than two hours (Fig. 5f, Fig. S17).

In order to view the role of G/CNT interlayer in efficiently prohibiting the diffusion of polysulfide anions, we carried out a visualized permeation test in a U-shaped glass cell, separated by G/CNT interlayer supported on polypropylene (PP) membrane (denoted as G/CNT/PP), 0.1 M of Li_2S_6 tetrahydrofuran (THF) solution on the left side of the

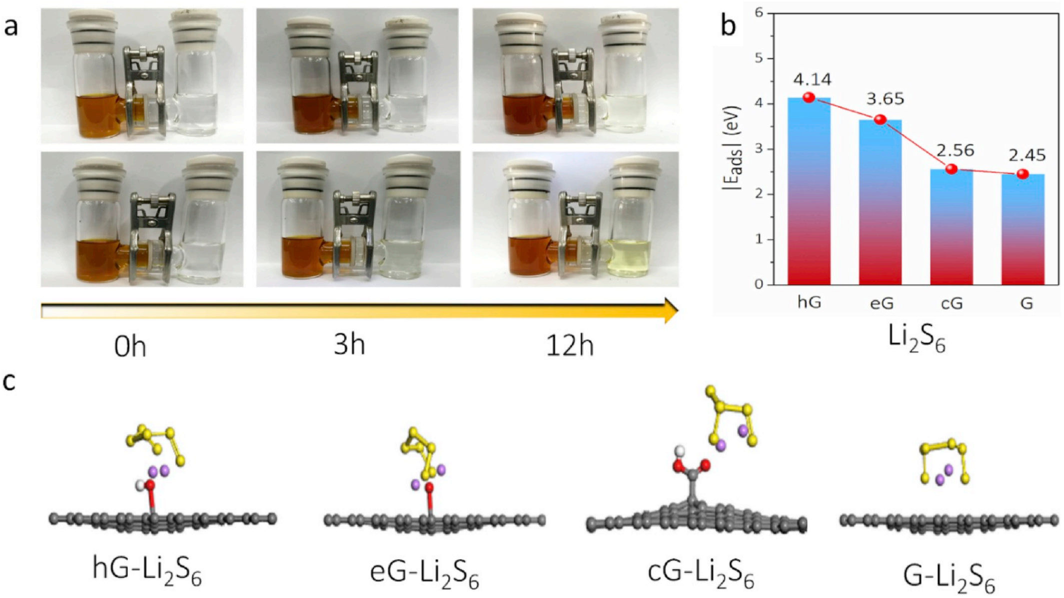

Fig. 6. (a) Polysulfide permeation measurements for G/CNT/PP (top) and individual PP (bottom) separators during the course of polysulfide diffusion from Li_2S_6/THF solution (left side) to pure THF (right side) of the U-shaped glass cell. (b) Theoretical absorption energy of Li_2S_6 interacted with hG, eG, zG and graphene (G), respectively. (c) Li_2S_6 adsorption geometries on hG, eG, cG and G (carbon, sulfur, oxygen, hydrogen and lithium atoms are represented by grey, yellow, red, white and purple, respectively).

tube, and a pure THF solvent in the right side of the tube. It is clearly observed that, from parallel comparison, the bare PP membrane (Fig. S18) disclosed negative effect on preventing the diffusion of Li_2S_6, and the THF solvent in right side of the tube turned yellow after 12 h (Fig. 6a bottom). However, the polysulfides of Li_2S_6 could hardly diffuse through the G/CNT/PP separator within 12 h (Fig. 6a top), demonstrating that G/CNT interlayer was an efficient anion-selectivity membrane for restraining the shuttling polysulfides. To clarify the interaction mechanism of Li_2S_6 with a G/CNT interlayer, we further performed the theoretical simulation of the interactions between Li_2S_6 molecules with pure graphene and graphenes with different oxygenated groups, including OH (hG), O (eG), COOH (cG) groups. Their adsorption energies in the final optimized structures of Li_2S_6 molecules on pure graphene, hG, eG and cG, respectively, are summarized in Fig. 6b and c. It is unveiled that hG (4.14 eV), eG (3.65 eV), cG (2.56 eV) disclosed higher adsorption energy than pure graphene (2.45 eV) to Li_2S_6. Therefore, it is demonstrated that the partly oxidized graphene was an efficient interlayer for polysulfide adsorption.

The remarkable volumetric capacity, volumetric energy density and enhanced long-term cyclability of Li—S batteries were mainly attributed to the advantages of G/CNT-S//G/CNT integrated cathode. First, the CNT cross-linked graphene network can provide outstanding mechanical flexibility, 3D interconnected porous structure, and rapid ionic/electronic transport, endowing high loading and efficient utilization of sulfur. Consequently, the free-standing sulfur-based electrode, free of polymer binder and metal current collector, can simultaneously improve the gravimetric/volumetric energy density, and cycling performance of Li—S batteries. Secondly, the compact G/CNT interlayer can substantially suppress the shuttling effect of lithium polysulfides *via* both chemical interaction and physical restriction. Thirdly, the mesoporous structure in the integrated film, with help of elastically bendable CNTs, can be readily manufactured to form the flexible, densely packed and conductive cathode with a high sulfur loading, which thereby can enhance the volumetric capacity, sufficiently reduce the volume change during the charge-discharge process and stabilize the cathode for long-life cyclability.

4. Conclusion

In summary, we developed a mechanically flexible, densely compact, electrically conductive and integrated cathode of G/CNT-S//G/CNT film, enabled by compressing 3D G/CNT-S aerogels as binder-free sulfur host and G/CNT film as internal current-collector interlayer, for Li—S batteries with record volumetric energy density and notably enhanced cyclability. The 3D G/CNT aerogels were prepared by a simple and cost-effective self-propagating combustion rapid reduction of GO/CNTs, and showed 3D interconnected porous network, large surface area, and high electrical conductivity. Using G/CNT aerogels simultaneously as both the host and interlayer, the integrated cathode delivered high capacity of 1286 mAh g^{-1} and 1841 Ah L^{-1}, and superior cycling stability. In particular, G/CNT-S//G/CNT cathode, at a sulfur loading of 1.64 g cm^{-3}, offered record volumetric energy density of 2482 Wh L^{-1} for Li—S battery cathodes reported to date. More importantly, our flexible integrated cathode is free of Al current collectors for Li—S batteries. Therefore, this proposed strategy will open numerous opportunities for constructing binder-free, current-collector-free, high-sulfur-loading and compact cathodes toward high-volumetric-energy-density and flexible Li—S batteries.

Conflicts of interest

The authors declare no competing financial interest.

Acknowledgment

This work was financially supported by the National Key R&D Program of China (Grants 2016YFB0100100, 2016YFA0200200), National Natural Science Foundation of China (Grants 51572259, 51872283, 21805273), Natural Science Foundation of Liaoning Province (Grant 20180510038), DICP (DICP ZZBS201708, DICP ZZBS201802), Dalian National Laboratory For Clean Energy (DNL), CAS, DICP&QIBEBT (DICP&QIBEBT UN201702), DNL Cooperation Fund, CAS (DNL180310, DNL180308), Exploratory Research Program of Shaanxi Yanchang Petroleum (Group) CO., LTD & DICP, and China Postdoctoral Science Foundation (Grants 2016M601349, 2017T100188).

Appendix A. Supplementary data

Supplementary data to this article can be found online at https://doi.org/10.1016/j.nanoen.2019.04.006.

References

[1] A. Manthiram, Y. Fu, S.H. Chung, C. Zu, Y.S. Su, Chem. Rev. 114 (2014) 117517 – 11787.
[2] H.J. Peng, J.Q. Huang, Q. Zhang, Chem. Soc. Rev. 46 (2017) 5237–5288.
[3] Y.M. Sun, N.A. Liu, Y. Cui, Nat. Energy 1 (2016) 16071.
[4] P.G. Bruce, S.A. Freunberger, L.J. Hardwick, J.M. Tarascon, Nat. Mater. 11 (2012) 19–29.
[5] D.N. Lei, K. Shi, H. Ye, Z.P. Wan, Y.Y. Wang, L. Shen, B.H. Li, Q.H. Yang, F.Y. Kang, Y.B. He, Adv. Funct. Mater. 28 (2018) 1707570.
[6] S.P. Wu, R.Y. Ge, M.J. Lu, R. Xu, Z. Zhang, Nanomater. Energy 15 (2015) 379–405.
[7] Y.X. Yin, S. Xin, Y.G. Guo, L.J. Wan, Angew. Chem. Int. Ed. 52 (2013) 13186–13200.
[8] H.L. Wu, L.A. Huff, A.A. Gewirth, ACS Appl. Mater. Interfaces 7 (2015) 1709–1719.
[9] C. Zheng, S.Z. Niu, W. Lv, G.M. Zhou, J. Li, S.X. Fan, Y.Q. Deng, Z.Z. Pan, B.H. Li, F.Y. Kang, Q.H. Yang, Nanomater. Energy 33 (2017) 306–312.
[10] Z.W. Seh, W.Y. Li, J.J. Cha, G.Y. Zheng, Y. Yang, M.T. McDowell, P.C. Hsu, Y. Cui, Nat. Commun. 4 (2013) 1331.
[11] L.M. Suo, Y.S. Hu, H. Li, M. Armand, L.Q. Chen, Nat. Commun. 4 (2013) 1481.
[12] G.M. Zhou, L. Li, D.W. Wang, X.Y. Shan, S.F. Pei, F. Li, H.M. Cheng, Adv. Mater. 27 (2015) 641–647.
[13] J. Pu, Z.H. Shen, J.X. Zheng, W.L. Wu, C. Zhu, Q.W. Zhou, H.G. Zhang, F. Pan, Nanomater. Energy 37 (2017) 7–14.
[14] A. Manthiram, S.H. Chung, C. Zu, Adv. Mater. 27 (2015) 1980–2006.
[15] N. Jayaprakash, J. Shen, S.S. Moganty, A. Corona, L.A. Archer, Angew. Chem. Int. Ed. 50 (2011) 5904–5908.
[16] X. Ji, K.T. Lee, L.F. Nazar, Nat. Mater. 8 (2009) 500–506.
[17] Z.Y. Lyu, D. Xu, L.J. Yang, R.C. Che, R. Feng, J. Zhao, Y. Li, Q. Wu, X.Z. Wang, Z. Hu, Nanomater. Energy 12 (2015) 657–665.
[18] G.M. Zhou, Y.B. Zhao, A. Manthiram, Adv. Energy Mater. 5 (2015) 1402263.
[19] H.F. Shi, S.Z. Niu, W. Lv, G.M. Zhou, C. Zhang, Z.H. Sun, F. Li, F.Y. Kang, Q.H. Yang, Carbon 138 (2018) 18–25.
[20] X.B. Cheng, J.Q. Huang, Q. Zhang, H.J. Peng, M.Q. Zhao, F. Wei, Nanomater. Energy 4 (2014) 65–72.
[21] Z. Yuan, H.J. Peng, J.Q. Huang, X.Y. Liu, D.W. Wang, X.B. Cheng, Q. Zhang, Adv. Funct. Mater. 24 (2014) 6105–6112.
[22] G.M. Zhou, S.F. Pei, L. Li, D.W. Wang, S.G. Wang, K. Huang, L.C. Yin, F. Li, Adv. Mater. 26 (2014) 625–631.
[23] L. Zhu, H.J. Peng, J.Y. Liang, J.Q. Huang, C.M. Chen, X.F. Guo, W.C. Zhu, P. Li, Q. Zhang, Nanomater. Energy 11 (2015) 746–755.
[24] P.Y. Zhai, H.J. Peng, X.B. Cheng, L. Zhu, J.Q. Huang, W. Zhu, Q. Zhang, Energy Storage Mater 7 (2017) 56–63.
[25] W.G. Chong, J.Q. Huang, Z.L. Xu, X.Y. Qin, X.Y. Wang, J.K. Kim, Adv. Funct. Mater. 27 (2017) 1604815.
[26] C. Tang, Q. Zhang, M.Q. Zhao, J.Q. Huang, X.B. Cheng, G.L. Tian, H.J. Peng, F. Wei, Adv. Mater. 26 (2014) 6100–6105.
[27] C.J. Hu, H.W. Chen, Y.B. Shen, D. Lu, Y.F. Zhao, A.H. Lu, X.D. Wu, W. Lu, L.W. Chen, Nat. Commun. 8 (2017) 479.
[28] Y.Z. Song, W. Zhao, N. Wei, L. Zhang, F. Ding, Z.F. Liu, J.Y. Sun, Nanomater. Energy 53 (2018) 432–439.
[29] Q. Sun, B.J. Xi, J.Y. Li, H.Z. Mao, X.J. Ma, J.W. Liang, J.K. Feng, S.L. Xiong, Adv. Energy Mater. 8 (2018) 1800595.
[30] X. Liu, J.Q. Huang, Q. Zhang, L.Q. Mai, Adv. Mater. 29 (2017) 1601759.
[31] Z.A. Ghazi, L.Y. Zhu, H. Wang, A. Naeem, A.M. Khattak, B. Liang, N.A. Khan, Z.X. Wei, L.S. Li, Z.Y. Tang, Adv. Energy Mater. 6 (2016) 1601250.
[32] J.R. He, Y.F. Chen, W.Q. Lv, K.C. Wen, C. Xu, W.L. Zhang, Y.R. Li, W. Qin, W.D. He, ACS Nano 10 (2016) 10981–10987.
[33] Z.Q. Li, C.X. Li, X.L. Ge, J.Y. Ma, Z.W. Zhang, Q. Li, C.X. Wang, L.W. Yin, Nanomater. Energy 23 (2016) 15–26.
[34] Z.B. Xiao, Z. Yang, L. Wang, H.G. Nie, M.E. Zhong, Q.Q. Lai, X.J. Xu, L.J. Zhang, S.M. Huang, Adv. Mater. 27 (2015) 2891–2898.
[35] J.Q. Huang, Q. Zhang, F. Wei, Energy Storage Mater 1 (2015) 127–145.
[36] L.Y. Chai, J.X. Wang, H.Y. Wang, L.Y. Zhang, W.T. Yu, L.Q. Mai, Nanomater. Energy 17 (2015) 224–232.
[37] W.L. Cai, G.R. Li, K.L. Zhang, G.N. Xiao, C. Wang, K.F. Ye, Z.W. Chen, Y.C. Zhu, Y.T. Qian, Adv. Funct. Mater. 28 (2018) 1704865.
[38] G.X. Li, Y. Gao, X. He, Q.Q. Huang, S.R. Chen, S.H. Kim, D.H. Wang, Nat. Commun. 8 (2017) 850.
[39] A. Sakuda, N. Taguchi, T. Takeuchi, H. Kobayashi, H. Sakaebe, K. Tatsumi, Z. Ogumi, Electrochem. Commun. 31 (2013) 71–75.
[40] H.L. Ye, L. Ma, Y. Zhou, L. Wang, N. Han, F.P. Zhao, J. Deng, T.P. Wu, Y.G. Li, J. Lu, Proc. Natl. Acad. Sci. U. S. A 114 (2017) 13091–13096.
[41] A. Douglas, R. Carter, L. Oakes, K. Share, A.P. Cohn, C.L. Pint, ACS Nano 9 (2015) 11156–11165.
[42] Y.L. Zhou, Y.L. Li, J. Yang, J. Tian, H.Y. Xu, J. Yang, W.L. Fan, ACS Appl. Mater. Interfaces 8 (2016) 18797–18805.
[43] Y.C. Jeong, J.H. Kim, S. Nam, C.R. Park, S.J. Yang, Adv. Funct. Mater. 28 (2018) 1707411.
[44] Q. Pang, X. Liang, C.Y. Kwok, J. Kulisch, L.F. Nazar, Adv. Energy Mater. 7 (2017) 1601630.
[45] R.P. Fang, S.Y. Zhao, S.F. Pei, X.T. Qian, P.X. Hou, H.M. Cheng, C. Liu, F. Li, ACS Nano 10 (2016) 8676–8682.
[46] M.W. Xiang, L. Yang, Y.F. Zheng, J. Huang, P. Jing, H. Wu, Y. Zhang, H. Liu, J. Mater. Chem. 5 (2017) 18020–18028.
[47] D.A. Dikin, S. Stankovich, E.J. Zimney, R.D. Piner, G.H. Dommett, G. Evmenenko, S.T. Nguyen, R.S. Ruoff, Nature 448 (2007) 457–460.
[48] H. Li, Y. Tao, C. Zhang, D.H. Liu, J.Y. Luo, W.C. Fan, Y. Xu, Y.Z. Li, C.H. You, Z.Z. Pan, M.C. Ye, Z.Y. Chen, Z. Dong, D.W. Wang, F.Y. Kang, J. Lu, Q.H. Yang, Adv. Energy Mater. 8 (2018) 1703438.
[49] M.D. Segall, P.J.D. Lindan, M. Probert, C.J. Pickard, P.J. Hasnip, S.J. Clark, M.C. Payne, J. Phys. Condens. Matter 14 (2002) 2717.
[50] B. Delley, J. Chem. Phys. 113 (2000) 7756–7764.
[51] J.A. White, D.M. Bird, Phys. Rev. B 50 (1994) 4954.
[52] J.P. Perdew, K. Burke, M. Ernzerhof, Phys. Rev. Lett. 77 (1996) 3865.
[53] H.J. Monkhorst, J.D. Pack, Phys. Rev. B 13 (1976) 5188.
[54] I.K. Moon, J. Lee, R.S. Ruoff, H. Lee, Nat. Commun. 1 (2010) 73.
[55] D. Yang, A. Velamakanni, G. Bozoklu, S. Park, M. Stoller, R.D. Piner, S. Stankovich, I. Jung, D.A. Field, C.A. Ventrice, R.S. Ruoff, Carbon 47 (2009) 145–152.
[56] J. Schuster, G. He, B. Mandlmeier, T. Yim, K.T. Lee, T. Bein, L.F. Nazar, Angew. Chem. Int. Ed. 51 (2012) 3591–3595.
[57] K.R. Paton, E. Varrla, C. Backes, R.J. Smith, U. Khan, A. O'Neill, C. Boland, M. Lotya, O.M. Istrate, P. King, T. Higgins, S. Barwich, P. May, P. Puczkarski, I. Ahmed, M. Moebius, H. Pettersson, E. Long, J. Coelho, S.E. O'Brien, E.K. McGuire, B.M. Sanchez, G.S. Duesberg, N. McEvoy, T.J. Pennycook, C. Downing, A. Crossley, V. Nicolosi, J.N. Coleman, Nat. Mater. 13 (2014) 624–630.
[58] Z.Y. Wang, Y.F. Dong, H.J. Li, Z.B. Zhao, H.B. Wu, C. Hao, S.H. Liu, J.S. Qiu, X.W. Lou, Nat. Commun. 5 (2014) 5002.
[59] Z.M. Cui, C.X. Zu, W.D. Zhou, A. Manthiram, J.B. Goodenough, Adv. Mater. 28 (2016) 6926–6931.
[60] Y.F. Dong, S.H. Zheng, J.Q. Qin, X.J. Zhao, H.D. Shi, X.H. Wang, J. Chen, Z.S. Wu, ACS Nano 12 (2018) 2381–2388.
[61] X.F. Yang, Y.Q. Chen, M.R. Wang, H.Z. Zhang, X.F. Li, H.M. Zhang, Adv. Funct. Mater. 26 (2016) 8427–8434.
[62] T.S.B. Tu, X. Chen, X.X. Zhao, M.R. Cheng, P.X. Xiong, Y.W. He, Q. Zhang, Y.H. Xu, Adv. Mater. 30 (2018) 1804581.
[63] L. Qie, A. Manthiram, Adv. Mater. 27 (2015) 1694–1700.
[64] G.M. Zhou, Y.B. Zhao, C.X. Zu, A. Manthiram, Nanomater. Energy 12 (2015) 240–249.
[65] P.T. Xiao, F.X. Bu, G.H. Yang, Y. Zhang, Y.X. Xu, Adv. Mater. 29 (2017) 1703324.
[66] F. Pei, L.L. Lin, D.H. Ou, Z.M. Zheng, S.G. Mo, X.L. Fang, N. F Zheng, Nat. Commun. 8 (2017) 482.

Haodong Shi obtained B.S. degree in Applied Chemistry from Northeastern University in 2016. He is pursuing the Ph.D. degree from Dalian Institute of Chemical Physics (DICP), Chinese Academy of Sciences (CAS), under the supervision of Prof. Zhong-Shuai Wu. His research interests focus on graphene & 2D materials for high-energy batteries.

Xuejun Zhao received her M.S. degree in Chemical Engineering from Dalian University of Technology in 2016. She is a research assistant in DICP, CAS. Her research focuses on graphene-based materials for lithium sulfur batteries.

Zhong-Shuai Wu received his Ph.D. degree in materials science from Institute of Metal Research, CAS in 2011. Then he worked as a postdoctor at Max-Planck Institute for Polymer Research from 2011 to 2015. Since June 2015, he joined DICP, CAS, and become a full Professor, and group leader of 2D Materials & Energy Devices. His research focuses on graphene and 2D materials for energy-related devices in supercapacitors, micro-supercapacitors, batteries and catalysis.

Yanfeng Dong received his Ph.D. degree in materials science from Dalian University of Technology in 2016. He worked as a postdoctor at DICP from 2016 to 2018. And now he is an associate professor at Northeastern University. His research focuses on graphene and 2D materials for advanced batteries e.g., lithium/sodium ion batteries and Li—S batteries.

Pengfei Lu received his Ph.D. degree from Yangzhou University in 2017. He currently works as a postdoctor in DICP, CAS. His research focuses on DFT calculations and MD simulations of graphene and 2D materials for advanced energy storage devices, e.g., supercapacitors and Li—S batteries.

Jian Chen received her Ph.D. in electrochemistry from Wuhan University in 1997. Then she worked as a postdoctor at Potsdam University in Germany from 1998 to 2000. Since October 2009, she was appointed as full Professor at DICP, CAS, and group leader of advanced secondary battery. her research interest is electrochemical transformation of energy, including lithium-sulfur batteries and lithium batteries.

Wencai Ren received his Ph. D. degree in materials science from Institute of Metal Research, CAS in 2005. He was promoted to be a professor of materials science at IMR, CAS since 2011. From 2009 to 2010, he worked with Prof. Andre K Geim at the University of Manchester as a visiting researcher. His current research interests include the synthesis, properties, and applications of graphene and other two-dimensional materials.

Hui-Ming Cheng received his PhD in Materials Science from the Institute of Metal Research, CAS. He worked at AIST and Nagasaki University in Japan, and MIT in USA, in the 1990s. Currently he is a Professor and Director of the *Advanced Carbon Research Division* of Shenyang National Laboratory for Materials Science, Institute of Metal Research, CAS, and the *Low-Dimensional Material and Device Laboratory* of the Tsinghua-Berkeley Shenzhen Institute, Tsinghua University. His research focuses on carbon nanotubes, graphene, two-dimensional materials, energy storage materials, photocatalytic semiconducting materials, and bulk carbon materials.

Xinhe Bao received his Ph.D. in Physical Chemistry from Fudan University in 1987. He held an Alexander von Humboldt Research Fellow position in Fritz-Haber Institute between 1989 and 1995, hosted by Prof. Gerhard Ertl. Following that, he joined DICP as a full Professor. He became a member of the CAS in 2009. His research interest is nano and interfacial catalysis, focusing on the fundamental understanding of heterogeneous catalysis, including development of new catalysts and novel catalytic processes related to energy conversion and storage.